

IIKL: Isometric Immersion Kernel Learning with Riemannian Manifold for Geometric Preservation

Zihao Chen, Wenyong Wang, *Senior Member, IEEE*, Jiachen Yang, Yu Xiang, *Member, IEEE*

Abstract—Previous research on geometric representation learning generally mapped non-Euclidean discrete data into Euclidean space, which may lead to the loss of critical intrinsic geometric and topological properties, resulting in distorted representations that fail to capture the underlying structure of the data. We propose a novel Isometric Immersion Kernel Learning (IIKL) method to build Riemannian manifold and isometrically induce Riemannian metric from non-Euclidean discrete data, and prove that isometric immersion is equivalent to the kernel function defined on the manifold's tangent spaces, which explicitly guarantees the invariance of the inner product between vectors in the arbitrary tangent space throughout the learning process, thus maintaining the geometric structure of the original data. Based on IIKL, we introduce a novel parameterized learning model together with an alternating training method derived from maximum likelihood estimation, ensuring efficient convergence of the new model. Experimental results demonstrated that IIKL successfully preserved the intrinsic geometric representation of data in both 3D and high-dimensional datasets, reducing the inner product invariant loss by over 90% compared to state-of-the-art methods. Additionally, it achieved an average 80% reduction in errors for geometric metrics related to isometric and conformal transformations, while also improved downstream reconstruction accuracy by 40%.

Index Terms— Geometric representation learning, Kernel function, Manifold learning, Riemannian geometry

I. INTRODUCTION

A recent study published in Nature highlights that researchers have recognized geometric manifold learning as a highly promising approach for extracting scientific representations from non-Euclidean discrete data, offering significant advantages for AI in scientific applications [1]. This approach facilitates the expression and learning of scientific representations with prior distributions, complex descriptors, and physical relationships in a compact and mathematically structured manner [2, 3].

Among those, in the study of scientific representation based on physical relations, the preservation of geometric and topological properties, has become a central focus in academic research, as these properties are crucial for capturing the intrinsic structure of data governed by fundamental physical

laws[4, 5]. A key mathematical tool in such circumstance is the inner product, which quantifies distances and angles etc basic metrics between discrete samples, revealing the geometric meaning within the vector space. Preserving geometric properties necessitates maintaining the invariance of specific inner product forms during the transformation of coordinate systems in the manifold learning process, making inner product invariance a critical consideration in the mathematical formulation of representation learning that emphasize preserving physical relationships. Currently, studies have shown that this invariance is crucial for revealing the fundamental physical principles underlying many scientific phenomena, such as symmetry and conservation laws[6, 7].

In computational science, the kernel function serves as a powerful tool for expressing inner product mappings, designed to preserve the invariance of the inner product structure during transformations across varying dimensional spaces. This approach enhances the effectiveness of resolving nonlinear problems while retaining the geometric and topological properties of the data [8]. Moreover, kernel functions can be integrated into representation learning methods that prioritize geometry preservation. In manifold learning, kernel methods can embed data into manifold spaces, where these physical relationships become more interpretable and easier to model. This approach has proven particularly beneficial in tasks such as classification, regression, and interpolation, where the preservation of spatial relationships is essential [9, 10].

Recently, there is growing recognition that the fusion of kernel methods with manifold geometries offers significant potential for improving representation learning by better capturing the complex geometric structures inherent in data. For instance, MultiL-KRIM [11] utilized kernel functions to model data as a point cloud on a manifold in reproducing kernel hilbert spaces(RKHS), effectively preserving geometric properties during data imputation. This approach, which integrates multiple kernel functions, improves approximation accuracy and provides a more intuitive alternative to traditional graph-Laplacian methods. The PLoM [12] method used a transient anisotropic kernel to improve statistical surrogates for stochastic manifold spaces, especially with heterogeneous data. By constructing a new vector basis that better captures statistical dependencies, this method enhances the accuracy of learned probability measures. While kernel functions significantly enhance manifold learning in capturing geometric representations, challenges remain in selecting appropriate prior kernel functions and building a parameterized model with universality for multiple specific

Zihao Chen, Wenyong Wang, Jiachen Yang, Yu Xiang are with the the University of Electronic Science and Technology (UESTC), Chengdu, China.(e-mail: chenzihao838@163.com, wangwy@uestc.edu.cn, 202321081101@std.uestc.edu.cn, jcxiaang@uestc.edu.cn).

applications[10, 13].

In this paper, the well-defined inner product structure within the tangent space of a Riemannian manifold provides a natural motivation for learning kernel functions within Riemannian spaces. In Riemannian geometry, the concept of isometric immersion refers to a geometric-preserving map between the tangent space of Riemannian manifolds, where the inner product-metric is maintained. This concept and the kernel function share the attempt to keep the inner product structure invariant during the mapping process, which inspires us to build an universal parameterized kernel-based manifold learning model with Riemannian geometry. We demonstrate that isometric immersion in the tangent space can be interpreted as a kernel function, followed by introducing the Isometric Immersion Kernel Learning (IIKL), which employs isometric immersion theorem as the inductive bias to induce a Riemannian metric that ensures the tangent mapping maintains inner product invariance from high-dimensional Euclidean space in a self-supervised manner. During the parameterization of the IIKL, we encountered a gap between the theoretical structure and practical implementation, which affected the convergence probability of the model. To address the issue, we proposed a soft-dual trick and ultimately employed the EM algorithm to resolve the mathematical model, deriving an alternating training method to guarantee that the model can be effectively trained and converged.

In the experimental section, we evaluated our approach from three key perspectives, using both 3D and high-dimensional discrete datasets to assess the model's performance in preserving geometric properties. First, we conducted a comprehensive evaluations analysis of the learned manifold structure, including an inner product invariance metric IPI we proposed. This is followed by a comparison with current state-of-the-art (SOTA) methods for geometry preservation, aiming to demonstrate the effectiveness of our approach. Second, we applied the learned Riemannian metrics to downstream tasks, illustrating the practicality of our method in real-world scenarios. This includes examining the model on 3D non-Euclidean point cloud datasets for reconstruction tasks and evaluating its performance on high-dimensional datasets for isometric and conformal transformations. Finally, we assessed the robustness and generalization capabilities of new model, conducting ablation studies on the soft-dual module and analyzing the impact of K-neighbor configurations in the tangent space approximation on the generalization of the kernel.

Contributions

1) We prove that isometric immersion is equivalent to the kernel function defined on the tangent spaces of Riemannian manifold. Building on this, we propose Isometric Immersion Kernel Learning (IIKL), which aim at inducing the Riemannian metric that keep inner product invariance in arbitrary tangent space during the transformation of spatial coordinate systems, thereby building a kernel function in the tangent space without requiring prior assumptions about the distribution of manifold space. The mathematical well-defined

inner product invariance promises that IIKL efficiently preserves the geometric representation of the original data throughout manifold learning.

2) We theoretically derive an alternating training framework for Isometric Immersion Kernel Learning, grounded in Maximum Likelihood Estimation (MLE). By leveraging isometric immersion as an inductive bias, the training framework theoretically guarantees that the learned kernel functions maintain the geometric properties of non-Euclidean discrete data when mapping them from high-dimensional Euclidean space to lower-dimensional Riemannian manifolds. During the parameterization process, we introduce the soft-dual module to address challenges arising from the inductive bias of isometric immersion, which can otherwise hinder the model's convergence probability.

3) We conducted a comprehensive evaluation of our method on both 3-dimensional and high-dimensional discrete point cloud datasets. Our approach, built on the principle of inner product invariance, demonstrated superior performance compared to state-of-the-art (SOTA) methods in preserving geometric properties. As part of this evaluation, we proposed the IPI metric, which quantify the inner product invariance of manifold learning methods. Specifically, the experimental results showed that the loss in isometric and conformal tasks related to inner product invariance was reduced by more than 80% compared to existing methods. Additionally, the downstream tasks (reconstruction and classification) utilizing the Riemannian metric learned by our model show improved performance.

II. RELATED WORKS

A. Geometric preserving manifold learning

Manifold learning is a specialized form of dimensionality reduction (DR), focused on uncovering the lower-dimensional representations embedded within high-dimensional data, by identifying and preserving the intrinsic geometric properties of data that reside on a continuous, non-linear manifold. Traditional manifold learning typically involved theoretically deriving the analytical distribution of data to obtain a precise representation on manifold[14, 15]. While encountering non-Euclidean discrete data lacks analytical distributions, The recognized approaches generally mapped it into a lower-dimensional Euclidean space, aiming to preserve local geometric structure[16]. Yet, this mapping often introduces distortions, as the Euclidean metric fails to preserve the complex, non-linear geometric relationships inherent in the original data distribution. Mathematically, the Euclidean metric's global linearity cannot capture the local curvature and non-linearity found in non-Euclidean spaces. This leads to distortions in key geometric properties, such as distances and angles, during dimensionality reduction[4]. Moreover, the inability of Euclidean metrics to preserve intrinsic geometric properties is not merely a theoretical issue but also a practical one. The process of DR in Euclidean space typically involves approximating complex geometric relationships using linear transformations. When data is mapped to Euclidean space, the

distances between points may be altered in a way that is not consistent with the underlying manifold structure, which violates the preservation of isometric properties[17].

Even in neural network-based methods, numerous studies still utilized DR in Euclidean space as learning objective to guide model training, which enhanced the robustness in real-world circumstances, while it also faced the distortion issues brought by Euclidean metric[18, 19]. Other studies made assumptions on the distribution of data's latent manifolds, which could simplify the manifold modeling process, whereas these assumptions might not reflect the real data distribution, leading to inaccuracies in representation and downstream inference[20, 21].

Previous studies have shown that although non-Euclidean data is represented in the original Euclidean space, its intrinsic representation exists on a latent low-dimensional manifold [20], thus, it is imperative to leverage non-Euclidean structures for the construction and learning of the representation in discrete samples. In this context, the mathematically well-defined Riemannian manifold emerges as a particularly promising candidate [22]. Compared with the Euclidean metric, the position-dependent Riemannian metric on the manifold fully utilizes the nonlinear characteristics of the space, preserving the geometric relationships among data in the DR process. With the Riemannian metric, a good computational framework could be built on the manifold, so that geometric metrics (e.g. Distance, Angle, Volume) and theories (e.g. Levi-Civita Connection and Ricci Curvature) can be defined mathematically. Nevertheless, nearly all manifold learning methods currently focus on deriving the DR mapping function from Euclidean space to Euclidean space, with no existing method capable of inducing the Riemannian metric from the original Euclidean space to build a true Riemannian manifold, where the latent representations could be mapped in a geometry-preserving manner.

B. Inner product preserving kernel methods

Kernel methods are essential in machine learning. They can attain inner product invariance when mapping vector data between high-dimensional and low-dimensional spaces, hence aiding in the preservation of geometric features in manifold learning. It allows for the efficient computation of inner products without explicitly working in high-dimensional spaces, alleviating the computational burden associated with the "curse of dimensionality[23]". The performance of kernel-based methods heavily depends on the choice of the predefined kernel, which may not be optimal for all data types or structures. Some studies have suggested that rotationally invariant kernels, such as RBF and inner product kernels, may induce a bias towards low-degree polynomials in high-dimensional settings. This bias arises because these kernels treat all dimensions equally, which limits their ability to capture more complex structures in the high-dimensional data[24]. While other studies have proposed high-order kernels can lead to overfit, as linear kernels may not capture sufficient data distribution complexity. A trade-off must be struck to optimize performance without overfitting[25].

With the development of neural networks, recently studies have proposed explicit data-driven kernel learning strategies. Paper[26] explored the application of neural networks to approximate functionals on RKHS. It established the universality of these approximations and derives explicit error bounds for various kernels, including inverse multiquadric, Gaussian, and Sobolev kernels. Paper[27] discussed deep kernel learning networks (DKL) that utilized random feature mapping to implement kernel methods as a two-layer neural network, enhancing nonlinear function approximation. The proposed methods demonstrated universal representation capabilities with minimal error, showcasing their effectiveness in both regression and classification tasks. These above methods allowed the kernel to be learned directly from the self-representation of the data, ensuring adaptive-weighting, which helps in overcoming the dependency on predefined kernels.

Overall, these paper concluded that Neural network-based models make significant progress in the field of kernel-based subspace clustering, offering a more flexible and effective approach to handling nonlinear data structures while preserving local manifold properties. However, Compared to the proposed IIKL method in this paper, existing learning-based methods lacked a strong geometric theoretical foundation, causing them incapable of establishing a model framework with theoretical interpretability and consequently falling short to verify the reliability of the learning results.

III. THEORETICAL FOUNDATIONS AND NEW INSIGHTS

In this section, we introduce the definitions of Riemannian geometry and kernel methods used in this paper. Based on these theoretical foundations, we give some new insights and propose the Isometric Immersion Kernel Learning (IIKL). For clarity, we present the notations along with their corresponding explanations in Table 1.

A. Theoretical Foundations in Geometry-preserving

Definition 1(Tangent map & pullback).

Let $f: \mathcal{M} \rightarrow \mathcal{N}$ be a smooth map between Riemannian manifolds. The tangent map $df: T_z\mathcal{M} \rightarrow T_{f(z)}\mathcal{N}$ at a point $z \in \mathcal{M}$ is the differential of f at z , which is a linear map from the tangent space $T_z\mathcal{M}$ to the tangent space $T_{f(z)}\mathcal{N}$.

Conversely, $pf: T_{f(z)}\mathcal{N} \rightarrow T_z\mathcal{M}$ is called the pullback of the smooth map f at point z , also the dual map of df .

Definition 2(Immersion).

A smooth map $f: \mathcal{M} \rightarrow \mathcal{N}$ between manifolds is called an immersion if its differential df is injective at $\forall z \in \mathcal{M}$. That is, df maps the tangent space $T_z\mathcal{M}$ injectively into the tangent space $T_{f(z)}\mathcal{N}$.

In Riemannian geometry, we generally seek an ideal immersion mapping that satisfies isometry to map the data on manifold \mathcal{M} to the manifold \mathcal{N} , because such mapping can preserve the geometric properties within the tangent space during the space transformation [28]. The definition of isometric mapping is as follows:

> REPLACE THIS LINE WITH YOUR MANUSCRIPT ID NUMBER (DOUBLE-CLICK HERE TO EDIT) <

Notation	Explanation
$T_z \mathcal{M}$	z is a point on the manifold \mathcal{M} , and $T_z \mathcal{M}$ is the tangent space consisting of all tangent vectors of z .
$U_z \mathcal{M}$	A neighborhood centered at z
$T \mathcal{M}$	The collection of all of the tangent spaces for all points on a manifold $\bigcup_{z \in \mathcal{M}} T_z \mathcal{M}$, called tangent bundle
$(\mathcal{M}, \mathcal{G})$	Let \mathcal{M} be a smooth Riemannian manifold. Given a smooth second-order covariant tensor field $\mathcal{G}_{\mathcal{M}}$ on \mathcal{M} , called the Riemannian metric of the Riemannian manifold \mathcal{M} .
$\mathcal{G}_{\mathcal{M}}[\mathbf{p}, \mathbf{q}]_{T_z}$	The inner product of $\mathbf{p}, \mathbf{q} \in T_z \mathcal{M}$ using the Riemannian metric $\mathcal{G}_{\mathcal{M}}$ assigns to point z
$\cdot _{T_z \text{ or } U_z}$	Property defined in the tangent space $T_z \mathcal{M}$ of z or a neighborhood $U_z \mathcal{M}$ approximating the tangent space
$\langle \dots \rangle$	Euclidean norm
$\xrightarrow{N=\mathbb{R}^d}$	Specify the Riemann manifold \mathcal{N} as a d -dimensional Euclidean space \mathbb{R}^d
df	A tangent map between two tangent spaces
pf	The pullback of the smooth map f , also the dual map of df

Table 1. Explanation of mathematical notations

Definition 3(Isometric immersion).

Let $f: (\mathcal{M}, \mathcal{G}) \rightarrow (\mathcal{N}, \mathcal{I})$ be an immersion between Riemannian manifolds. If the map satisfies follow equation at $\forall z \in \mathcal{M}$,

$$\mathcal{G}_{\mathcal{M}}[\mathbf{p}, \mathbf{q}]_{T_z} = \mathcal{I}(df(\mathbf{p}), df(\mathbf{q})), \quad (1)$$

where $\mathcal{G}_{\mathcal{M}}$ and \mathcal{I} represent the Riemannian metrics of manifolds \mathcal{M} and \mathcal{N} (if \mathcal{N} is considered as a Euclidean space \mathbb{R}^d , then \mathcal{I} is a Euclidean metric, thus $\mathcal{I}(df(\mathbf{p}), df(\mathbf{q})) = \langle df(\mathbf{p}), df(\mathbf{q}) \rangle_{\mathbb{R}^d}$), then f is an isometric immersion.

This implies that f preserves the geometric properties during the mapping.

In other words, isometric immersion is about finding a suitable metric $\mathcal{G}_{\mathcal{M}}$ that maintains the invariance of the inner product between arbitrary vectors $\mathbf{p}, \mathbf{q} \in T_z \mathcal{M}$ at $\forall z \in \mathcal{M}$ under the tangent mapping df .

Definition 4(Induced metric).

The induced metric is the position-dependent symmetric positive-definite matrix defined at $\forall z \in \mathcal{M}$, on a manifold \mathcal{M} , that is induced from the metric tensor \mathcal{I} on manifold \mathcal{N} into which the \mathcal{M} is immersed (or embed), through the pullback pf .

$$\begin{aligned} \mathcal{G}_{\mathcal{M}}|_{T_z} &= pf|_{T_z} \circ \mathcal{I} \\ pf|_{T_z} \circ \mathcal{I} &= (pf|_{T_z} \cdot pf|_{T_z}^T) \mathcal{I} = (df|_{T_z}^T \cdot df|_{T_z}) \mathcal{I} \\ \text{s.t. } pf &= df^T, \end{aligned} \quad (2)$$

where \mathcal{I} is generally a Euclidean metric in actual scenarios, and since the tangent map df and pullback pf are a pair of linear maps that satisfy the duality relationship, thus they can

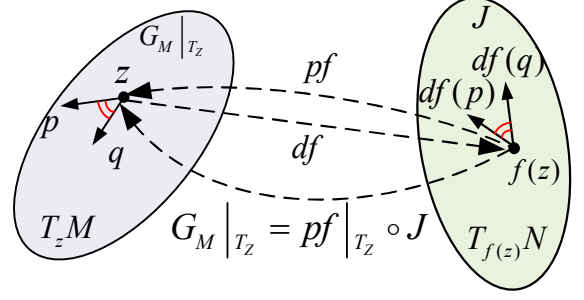


Figure 1: Mapping relationships between two tangent spaces. We use red horizontal line to indicate that the two vectors satisfies isometry.

be replaced by transposition $pf = df^T$.

We intuitively transform above definitions into a visualization in Fig. 1.

Next, we provide some basic concepts and definitions about kernel methods:

Definition 5(Kernel Function).

A kernel function $\mathcal{K}(\mathbf{p}, \mathbf{q})_W$ defines a measure of similarity between samples $\forall \mathbf{p}, \mathbf{q} \in W$ in space W , often by implicitly mapping these points to a higher-dimensional inner product space \mathcal{V} . Formally, a kernel function computes the inner product between vectors $\varphi(\mathbf{p})$ and $\varphi(\mathbf{q})$ in the space \mathcal{V} , as follows:

$$\mathcal{K}(\mathbf{p}, \mathbf{q})_W = \langle \varphi(\mathbf{p}), \varphi(\mathbf{q}) \rangle_{\mathcal{V}}, \quad (3)$$

This implicitly defined function $\varphi: W \rightarrow \mathcal{V}$ exists whenever the space \mathcal{V} can be equipped with a suitable inner product metric ensuring the function \mathcal{K} satisfies Mercer's condition. The Mercer's condition states that if a kernel function \mathcal{K} is symmetric, continuous and leads to a positive semi-definite kernel matrix then there exists a function φ that maps \mathbf{p} and \mathbf{q} into another space while satisfy $\mathcal{K}(\mathbf{p}, \mathbf{q})_W = \langle \varphi(\mathbf{p}), \varphi(\mathbf{q}) \rangle_{\mathcal{V}}$.

B.Isometric Immersion Kernel Learning**Corollary 1(Isometric Immersion Kernel).**

The isometric immersion f in (1) could be interpreted as the kernel function over the tangent space $T_z \mathcal{M}$ at $\forall z \in \mathcal{M}$, i.e. Isometric immersion could be viewed as the kernel function defined in the tangent bundle $T \mathcal{M}$, which preserves the invariance of the inner product between vectors within arbitrary tangent space $T_z \mathcal{M}$. This leads to the following equivalence at $\forall z \in \mathcal{M}$, in which $\mathcal{G}_{\mathcal{M}}$ represents the Riemann metric in the tangent space $T_z \mathcal{M}$:

$$\begin{aligned} \mathcal{K}(\mathbf{p}, \mathbf{q})_W &= \mathcal{G}_{\mathcal{M}}[\mathbf{p}, \mathbf{q}]_{T_z} \\ \text{s.t. } W &\equiv T_z \mathcal{M}, \quad \mathcal{V} \equiv \mathcal{N}, \quad \varphi \equiv df \end{aligned} \quad (4)$$

Proof:

Assume that the tangent space $T_z \mathcal{M}$ is equivalent to the input space W in (3), $W \equiv T_z \mathcal{M}$, and the Euclidean space \mathcal{N} is equivalent to the inner product space \mathcal{V} in (3), $\mathcal{V} \equiv \mathcal{N}$. Also, the coordinate transformation φ within the kernel function is defined as the differential df of the isometric immersion map in the tangent space, $\varphi \equiv df$. Then, based on these equivalence relations, we have:

$$\langle \varphi(\mathbf{p}), \varphi(\mathbf{q}) \rangle_{\mathcal{V}} = \mathcal{I}(df(\mathbf{p}), df(\mathbf{q}))$$

> REPLACE THIS LINE WITH YOUR MANUSCRIPT ID NUMBER (DOUBLE-CLICK HERE TO EDIT) <

z_h , which denote as $U_{z_h}\mathcal{M}$, and the neighborhood after decoder mapping, which denote as $U_{f_D^\theta(z_h)}\mathcal{M}$, must be injective. According to the Definition 2, the f_D^θ can be regarded as an immersion from $U_{z_h}\mathcal{M}$ to $U_{f_D^\theta(z_h)}\mathcal{M}$.

To achieve immersion, we uses the reconstruction constraints of the AE to make the decoder to approximately satisfy the immersion conditions:

Immersion Loss. To ensure that the AE follows the nearly homeomorphism, so that f_D^θ satisfies immersion. It is essential to have the output $x^r = f_D^\theta(z)$ to reconstruct input data x as accurately as possible:

$$\mathcal{L}_{re}(\theta) = \mathbb{E}_x[x - f_D^\theta(f_E^\theta(x))]^2 \quad (9)$$

Proof of Rieamannian Metric Legitimacy. According to Definition 4, a decoder f_D^θ that satisfies the immersion condition can induce the Riemannian metric. For theoretical rigor, we prove the legitimacy of the Riemannian metric induced from the parameterized module (8), and demonstrate that this metric must satisfy the Mercer's condition in the kernel method. Take a 2-dimensional Riemann manifold as an example.

Given an ideal Autoencoder in objective (8). Where x is the input of encoder f_E^θ in original space \mathcal{N} (dimension $d \geq 2$), and the output is the latent sample in 2-dimensional manifold space \mathcal{M} . The f_D^θ denotes a decoder with 2-dimensional input and d -dimensional output. It could be seen that f_E^θ and f_D^θ are inverse mappings of each other and are both bijective. The Riemannian metric at point z_h on the manifold \mathcal{M} can be obtained using the differential of f_D^θ at that point according to the metric induce (2):

$$\mathcal{G}_{\mathcal{M}}|_{T_{z_h}} = df_D^\theta|_{T_{z_h}}^T \cdot df_D^\theta|_{T_{z_h}} \quad (10)$$

Expanding the above formula, we get:

$$\begin{aligned} \frac{\partial \vec{R}|_{z_h}}{\partial v} &= \vec{e}_v|_{z_h} = \frac{\partial c_1}{\partial v} \vec{e}_{c_1} + \frac{\partial c_2}{\partial v} \vec{e}_{c_2} + \frac{\partial c_3}{\partial v} \vec{e}_{c_3} + \dots + \frac{\partial c_d}{\partial v} \vec{e}_{c_n} \\ \frac{\partial \vec{R}|_{z_h}}{\partial u} &= \vec{e}_u|_{z_h} = \frac{\partial c_1}{\partial u} \vec{e}_{c_1} + \frac{\partial c_2}{\partial u} \vec{e}_{c_2} + \frac{\partial c_3}{\partial u} \vec{e}_{c_3} + \dots + \frac{\partial c_d}{\partial u} \vec{e}_{c_n} \\ \mathcal{G}_{\mathcal{M}}|_{T_{z_h}} &= \begin{bmatrix} \vec{e}_u|_{z_h} \cdot \vec{e}_u|_{z_h} & \vec{e}_u|_{z_h} \cdot \vec{e}_v|_{z_h} \\ \vec{e}_v|_{z_h} \cdot \vec{e}_u|_{z_h} & \vec{e}_v|_{z_h} \cdot \vec{e}_v|_{z_h} \end{bmatrix}, \end{aligned} \quad (11)$$

where $\vec{R}|_{z_h}$ represents an arbitrary curve at point z_h , $\vec{e}_v|_{z_h}$ and $\vec{e}_u|_{z_h}$ are the local coordinate cards of point z_h in manifold space \mathcal{M} , and $c_1 \sim c_d$ is the coordinate card in the original space \mathcal{N} .

Then we verify the legitimacy of the induced Riemannian metric $\mathcal{G}_{\mathcal{M}}|_{T_{z_h}}$: Whether the metric matrix (11) meets positive and symmetric as described in Definition (4).

From (11), we see that the Riemannian metric induced by the AE obviously satisfies the symmetric property. For the positive definiteness condition, we need to prove that the Leading Principle Minors in the metric tensor matrix (11) are all positive.

With proof by contradiction (in the supplementary material), we prove that if the immersion loss \mathcal{L}_{re} is sufficiently low and the issue of neuron death in the final hidden layer of the encoder f_E^θ is avoided, the Positive definiteness of the

Riemannian metric could be guaranteed. Consequently, in constructing the network, we abstain from using ReLU activation functions that may result in neuron death. Therefore, we set the kernel function $\mathcal{K} = \mathcal{G}_{\mathcal{M}}|_{T_{z_h}}$ in the tangent space at z_h . According to the above derivation, the Riemannian metric $\mathcal{G}_{\mathcal{M}}|_{T_{z_h}}$ satisfies the positive definite symmetry property, so \mathcal{K} is a semi-positive definite function that satisfies the Mercer condition, that is, a kernel function in the tangent space $T_{z_h}\mathcal{M}$ as (4).

b. Isometric Module

Tangent Space Approximation. Previous studies have found that when the distance between neighboring points on the manifold is close enough, the geodesic distance between them can be approximately considered as the Euclidean distance. Therefore, current learning models generally use the neighborhood space $U_{z_h}\mathcal{M}$ of z_h , which composed of its K nearest samples to approximate the tangent space $T_{z_h}\mathcal{M}$ [29].

However, when the number of nearest neighbor points K is set too big, the distance between the samples may become too great, leading to an increased approximation error. To solve this problem, some studies proposed to resample around the origin point of the tangent space and use regularization terms to constrain the distance between these samples to be close enough [30]. Nonetheless, these regularizations impose higher computational demands in high-dimensional scene datasets, hence, in this study, we still choose to use a neighborhood $U_{z_h}\mathcal{M}$ composed of K nearest neighbors to approximate the tangent space $T_{z_h}\mathcal{M}$. For the rigor of the study, we will comprehensively examine the impact of the choice of K on the generalization of the model in the experimental part.

Isometric loss. Inspired by (1), ideally, the isometric loss should be calculated as follows (12), in which we set π as a customizable sampling distribution in the neighborhood $U_{z_h}\mathcal{M}$. The sampling set $S(z_h) \in U_{z_h}\mathcal{M}$ could be obtained by performing π , for $\forall \mathbf{p}, \mathbf{q} \in S(z_h)$:

$$\mathcal{L}(\theta) = \mathbb{E}_{z, S(z_h) \sim \pi} \{ \mathcal{G}_{\mathcal{M}}^\theta[\mathbf{p}, \mathbf{q}]_{U_{z_h}} - \mathcal{I}(df_D^\theta(\mathbf{p})_{U_{z_h}}, df_D^\theta(\mathbf{q})_{U_{z_h}}) \}^2, \quad (12)$$

where $\mathcal{G}_{\mathcal{M}}^\theta = \mathcal{P}f_D^\theta|_{U_{z_h}} \cdot \mathcal{P}f_D^\theta|_{U_{z_h}}^T$, and decoder f_D^θ forms an immersion mapping, the Riemannian metric on the manifold could be obtained with the (10). The ideal situation is to identify a parameterized f_D^θ that meets both isometry and immersion conditions. i.e. the parameter $\omega = \theta$ of the parameterized module in the (7), we will refer to this situation as ‘‘hard-dual model’’ in the following text. However, we found that such ideal f_D^θ is impractical, as requiring it to satisfy both isometry and immersion could potentially decrease the likelihood of model convergence, which will be observed in the experiments part.

To address this issue, we propose a trick of separating the map f_D^θ and its pullback $\mathcal{P}f_\varphi^\omega$ with individual parameters set θ and ω . According to Definition 1, the $\mathcal{P}f_\varphi^\omega$ should be the dual of the df_D^θ . Constructing them separately ignores this dual bond and introduce dual loss, therefore we call it the soft-dual

Algorithm 1: Isometric immersion kernel learning**Input:** Discrete dataset \mathcal{X} .**Parameter:** Initialize the parameters ω and θ in encoder f_E^θ , decoder f_D^θ , and the soft-dual pullback f_φ^ω . Set a concrete neighborhood sampling distribution π and hyperparameter set $\{\alpha, \gamma, \varepsilon\}$.**Output:** $f_E^\theta, f_D^\theta, f_\varphi^\omega$, through the differential of f_φ^ω to obtain the Riemannian metric $\mathcal{G}_\mathcal{M}^\omega$ on the manifold \mathcal{M} .1: **For** iteration $< \max \text{ iter number}$ **do**:2: Input the mini-batch x into the encoder, and the latent code $z = f_E^\theta(x)$ is obtained.3: Perform sampling π in the neighborhood of z_h to obtain the sampling set $S(z_h)$.4: **For** iteration $< \max \text{ iter_imm number}$ **do**:5: Input $S(z_h)$ into the decoder6: Calculate loss $\mathcal{L}_{\text{immersion}}(\theta) = \alpha \mathcal{L}_{re}(\theta) + \gamma \mathcal{L}_{du,d}(\theta)$.7: ADAM optimization of parameter θ .8: **For** iteration $< \max \text{ iter_iso number}$ **do**:9: The Riemannian metric $\mathcal{G}_\mathcal{M}^\omega$ can be obtained by calculating $\mathcal{G}_\mathcal{M}^\omega = \mathcal{P}f_\varphi^\omega|_{T_{z_h}} \cdot \mathcal{P}f_\varphi^\omega|_{T_{z_h}}^T$.10: Calculate loss $\mathcal{L}_{\text{isometry}}(\omega) = \varepsilon \mathcal{L}_{is}(\omega) + \gamma \mathcal{L}_{du,\varphi}(\omega)$.11: ADAM optimization of parameter ω .12: **return** $f_E^\theta, f_D^\theta, f_\varphi^\omega, \mathcal{G}_\mathcal{M}^\omega$

trick. According to (2), the Riemannian metric in \mathcal{L}_{is} could be calculated from f_φ^ω 's pullback:

$$\mathcal{G}_\mathcal{M}^\omega|_{U_{z_h}} = \mathcal{P}f_\varphi^\omega|_{U_{z_h}} \cdot \mathcal{P}f_\varphi^\omega|_{U_{z_h}}^T \quad (13)$$

Then the isometric loss could be rewritten as:

$$\mathcal{L}_{is}(\omega) = \mathbb{E}_{z, S(z_h) \sim \pi} \{ \mathcal{G}_\mathcal{M}^\omega[\mathbf{p}, \mathbf{q}]_{U_{z_h}} - \mathcal{J}(df_D^\theta(\mathbf{p})_{U_{z_h}}, df_D^\theta(\mathbf{q})_{U_{z_h}}) \}^2$$

$$\xrightarrow{\mathcal{N}=\mathbb{R}^d} \mathbb{E}_{z, S(z_h) \sim \pi} \{ \mathcal{G}_\mathcal{M}^\omega[\mathbf{p}, \mathbf{q}]_{U_{z_h}} - \langle df_D^\theta(\mathbf{p})_{U_{z_h}}, df_D^\theta(\mathbf{q})_{U_{z_h}} \rangle_{\mathbb{R}^d} \}^2 \quad (14)$$

We generally assume that the the original high-dimensional space \mathcal{N} , where the original data exists, is a d -dimensional Euclidean space \mathbb{R}^d , hence, the aforementioned inner product could be expressed in the form of an inner product within the Euclidean space $\langle \cdot, \cdot \rangle_{\mathbb{R}^d}$. It should be noted that $\mathcal{G}_\mathcal{M}^\omega[\mathbf{p}, \mathbf{q}]_{U_{z_h}}$ in (14) could be instead by $\mathcal{K}[\mathbf{p}, \mathbf{q}]_{U_{z_h}}$, which is considered the loss derived from the kernel function in the approximate tangent space $U_{z_h}\mathcal{M}$.

The isometric loss is the key to maintaining the invariance of the inner product. Intuitively, we can understand that the inner product operation measures the similarity between vectors between high-dimensional vectors. This similarity is also a kind of distance property, and the isometric loss is the regularization that maintains this property.

c. soft-dual Module

During training, the decoder f_D^θ reconstructs the original data as accurately as possible to meet the immersion mapping of Definition 2, while the mapping f_φ^ω seeks to learn the induced Riemannian metric equipped in the tangent space satisfy (1) to ensure that the immersion mapping df_D^θ adheres to the definition of isometry.

To intuitively control the dual bond between $\mathcal{P}f_\varphi^\omega$ and df_D^θ , we propose parameterizing f_φ^ω . Theoretically, f_φ^ω is the copy of f_D^θ , but for practical feasibility of isometry concept, we train f_φ^ω and f_D^θ with independent network parameters. The soft-dual loss is separated into two parameterized module

losses.

For f_D^θ , the loss function is:

$$\mathcal{L}_{du,d}(\theta) = \mathbb{E}_z (\|f_D^\theta(z) - f_\varphi^\omega(z)\|), \quad (15)$$

where the parameter ω in f_φ^ω is fixed, and the f_D^θ is optimized. The lower the loss $\mathcal{L}_{du,d}$, the stronger the dual bond between df_D^θ and $\mathcal{P}f_\varphi^\omega$.

Similarly, For f_φ^ω , there is:

$$\mathcal{L}_{du,\varphi}(\omega) = \mathbb{E}_z (\|f_D^\theta(z) - f_\varphi^\omega(z)\|), \quad (16)$$

where we fix the parameter θ in f_D^θ , optimize f_φ^ω .

Combined with the model convergence experiment in the following text, soft-dual loss is a module that controls the isometric immersion inductive bias of the model, allow us to trade-off between training convergence efficiency (weaker dual strength) and theoretical rigor (stronger dual strength).

C.Training Methods

We bring the symbols in the parameterized modules above into the MLE modeling (7) of the IIKL:

$$\argmax_{\omega, \theta} \sum_r \ell n [\sum_r \mathcal{P}((\mathcal{G}_\mathcal{M}^\dagger|_{U_{z_h}}; \omega), (df_D^\dagger|_{U_{z_r}}; \theta))], \quad (17)$$

where $\mathcal{G}_\mathcal{M}^\dagger|_{U_{z_h}} = \mathcal{P}f_\varphi^\omega|_{U_{z_h}} \cdot \mathcal{P}f_\varphi^\omega|_{U_{z_h}}^T$, the $df_D^\dagger|_{T_{z_r}}$ represents mapping f_D^θ in the neighborhood of z_r . We propose to leverage the EM algorithm to solve the (17). The complete derivation and a convergence proof of this model are all included in the supplementary materials. Below we only give the conclusion of the derivation:

In step E:

$$\theta^{k+1} = \argmax_\theta \mathcal{P}[(df_D^\dagger|_{U_z}; \theta^k) | (\mathcal{G}_\mathcal{M}^\dagger|_{U_z}; \omega^j)], \quad (18)$$

where the conditional probability \mathcal{P} implies that we fix parameter ω^j of the $\mathcal{G}_\mathcal{M}^\dagger$, and update the parameter θ^{k+1} in immersion's tangent mapping df_D^\dagger .

In step M:

$$\omega^{j+1} = \argmax_\omega \sum_h \ell n \mathcal{P}[(\mathcal{G}_\mathcal{M}^\dagger|_{U_{z_h}}; \omega^j) | (df_D^\dagger|_{U_z}; \theta^k)], \quad (19)$$

where, similarly, the conditional probability \mathcal{P} implies that the

> REPLACE THIS LINE WITH YOUR MANUSCRIPT ID NUMBER (DOUBLE-CLICK HERE TO EDIT) <

parameter θ^k is fixed, and we update the parameter ω^{j+1} in the \mathcal{G}_M^\dagger .

Intuitively, the entire network is updated alternately. The approximate process of immersion is optimized in step E to ensure that the mapping $\mathcal{d}f_d^\dagger$ meets the immersion condition. The corresponding loss function to this part is:

$$\mathcal{L}_{immersion}(\theta) = \alpha \mathcal{L}_{re}(\theta) + \gamma \mathcal{L}_{du,d}(\theta), \quad (20)$$

where α, γ denote the hyperparameters. When $\mathcal{d}f_d^\dagger$ holds true, $\mathcal{L}_{immersion}$ should be nearly 0.

For the M step, under the premise that the immersion mapping is legal, a pullback $\mathcal{p}f_\phi^\omega$ is sought so that the pullback metric \mathcal{G}_M^\dagger induced by it can ensure that f_d^\dagger satisfies isometric condition, i.e. construct a legal kernel function mapping in the tangent space. The loss function corresponding to this part is:

$$\mathcal{L}_{isometry}(\omega) = \varepsilon \mathcal{L}_{is}(\omega) + \gamma \mathcal{L}_{du,\phi}(\omega), \quad (21)$$

where ε, γ denote the hyperparameters controlling the trade-off. When \mathcal{G}_M^\dagger holds true, $\mathcal{L}_{isometry}$ should be nearly 0.

Consequently, the comprehensive loss function of the novel model could be expressed as:

$$\min_{\omega} \min_{\theta} \mathcal{V}(\omega, \theta) = \mathcal{L}_{immersion}(\theta) + \mathcal{L}_{isometry}(\omega) \quad (22)$$

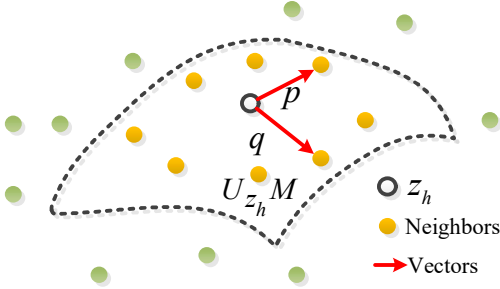


Figure 3: The vector in the approximate tangent space consists of the origin and its neighbors

V. EXPERIMENTS RESULT AND ANALYSIS

All experiments are divided into 3 parts: A. Geometric-preserving Evaluations to investigate the geometric preservation capability of the novel model for non-Euclidean discrete data. B. Downstream tasks of the learned Riemannian metric to observe the influence of the learned Riemann metric

on downstream tasks. C. Model Validity Studies to validate the model's generalization.

Datasets. To comprehensively evaluate the learning efficacy of the new model and its impact on downstream tasks, we selected two types of datasets: high-dimensional discrete data and 3-dimensional point cloud data for simulation experiments, demonstrating the model's performance on datasets with different feature dimensions. We selected 3D surface unstructured point cloud datasets for experiments, such as TOSCA[31] and DLR-F11[32] published datasets. In the TOSCA, we selected the point cloud structures of humans (No personally identifiable information is involved), cats, and gorillas as learning objects. We extracted 800 to 2000 3D points of the object as the training set. In the DLR-F11 airfoil dataset, the shape of a half fuselage with an airfoil in the form of polynomial surface control points was provided. With the Bessel surface analytical expression of the wing shape, we obtained an unstructured point cloud training set consisting of 1,000 points on the airfoil based on random sampling of the analytical expression, as shown in Fig. 4 (a) (b).

For high-dimensional datasets, we selected the network attack traffic datasets CIC-DDoS2019 and CIC-IDS2018 with classification labels, which contain a variety of DDoS attack types. There are papers that introduce the attack cycles, attack network topologies, etc. of specific attack types about these datasets[33]. After data cleaning, the CIC-DDoS2019 with the feature of 68-dimensional, and CIC-IDS2018 with the feature of 69-dimensional. In order to save computing resources, we randomly retained 2,500 high-dimensional discrete samples as the training set of each dataset.

Baselines. We conducted experiments on the new model and various well-accepted baselines, including: LLE[34], MLL[35], LTSA[36], t-SNE[37], UMAP[16], TriMAP[38], Spectral[39], ISOMAP[40], PaCMAP[41], CAMEL[42], DTR_AE[43], and inv-ML[44]. According to the model category, they are divided into local geometry preserving methods, global geometry preserving methods, and geometric prior methods. Among them, the methods in geometric prior are worth noting. DTR_AE and inv_ML use Representation Topology Divergence and locally isometric smoothness as model regularization constraints respectively, while CAMEL uses approximate curvature invariance to constrain the model's representation learning process. All three are representative SOTA models in geometry-preserving manifold learning

Paramete type	Paramete name	Value
Hardware platform	GPU	Two NVIDIA RTX 4090 GPUs
Software platform	Program language	Python 3.8.10
	Deep learning framework	Pytorch 1.11.0
Hyperparameters of models	Optimization algorithm	Adam(Beta1=0.9 and Beta2=0.999)
	Data normalization	Max-min normalization
	Activation function	LeakyReLU
	Batch normalization	Yes
	Batch size	100
	Learning rate	0.0001
	Epochs	1000
	Validation	5-fold cross validation
	Default training set:validation set	8:2
	Hyperparameters set $\{\alpha, \gamma, \varepsilon\}$ value range	$\alpha:[1,10,100], \gamma:[1,10,100], \varepsilon:[0.5,1]$

Table 2: Hyperparameters and hardware configuration in the experiments

> REPLACE THIS LINE WITH YOUR MANUSCRIPT ID NUMBER (DOUBLE-CLICK HERE TO EDIT) <

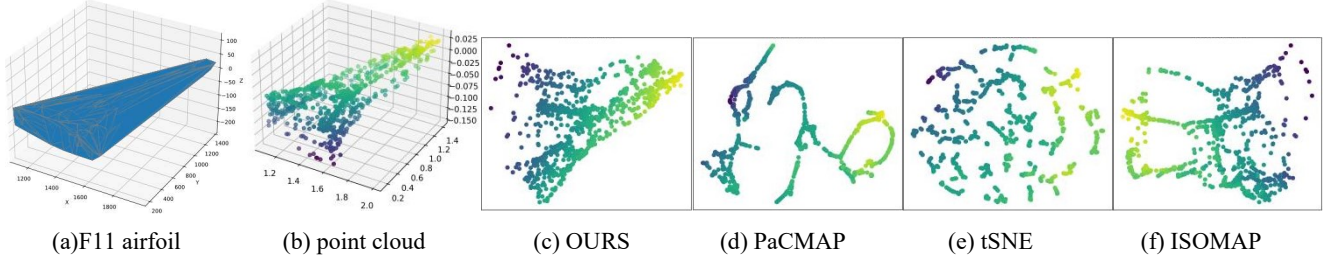


Figure 4: A comparison of various manifold learning methods on F11 airfoil point cloud

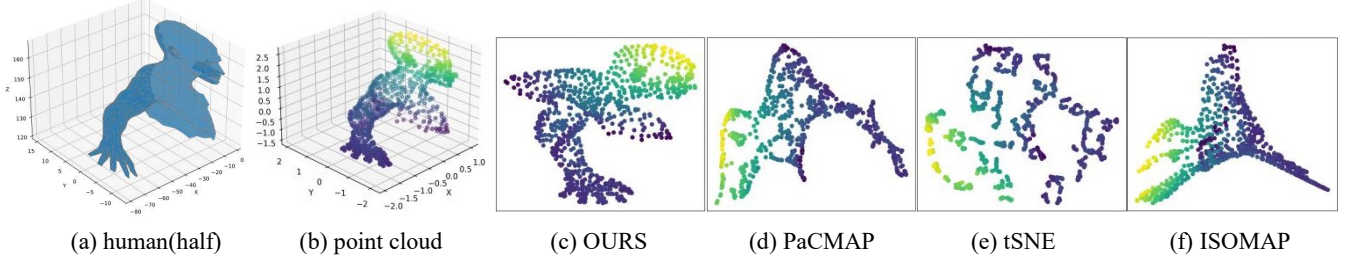


Figure 5: A comparison of various manifold learning methods on human (in TOSCA) point cloud

Type		Global structure		Local structure		Both	Curvature	Avg score
		Triplet	SpearCor	Npp	Nnwr	Auc	Curv sim	
Local Methods	LLE	0.528	0.019	0.093	0.053	0.116	0.767	0.262
	MLLE	0.523	0.068	0.079	0.043	0.104	0.813	0.272
	LTSA	0.543	0.151	0.019	0.002	0.030	0.756	0.250
	tSNE	0.627	0.328	0.693	0.812	0.497	0.515	0.579
	UMAP	0.510	0.024	0.586	0.691	0.349	0.010	0.360
	TriMAP	0.737	0.612	0.433	0.485	0.447	0.623	0.556
Global Methods	Spectral	0.572	0.301	0.396	0.417	0.257	0.759	0.450
	ISOMAP	0.752	0.709	0.494	0.484	0.504	0.832	0.629
	PaCMAP	0.745	0.572	0.555	0.631	0.475	0.305	0.547
Geometric Methods	CAMEL	0.655	0.411	0.422	0.423	0.357	0.548	0.469
	<i>inv_ML</i>	0.747	0.792	0.801	0.858	0.587	0.962	0.791
	<i>DTR_AE</i>	0.841	0.887	0.858	0.935	0.695	0.942	0.860
	OURS	0.859	0.922	0.871	0.942	0.713	0.977	0.881

Table 3: Comparative experiments of manifold learning evaluations on the CIC-IDS2018. The best and second/third best results are emphasized in underlined and **bold** cases.

proposed recent years.

Implementation Details. In the geometry-preserving evaluation experiments, we followed the same experimental settings as Liu's previous work [42]. For more detailed model structures and hyperparameter settings, please refer to the Table 2. All experimental results without confidence intervals are the means of 5 independent repeated experiments.

Here, we provide a method to concertize the sampling method π for the new model. We take tangent vectors formed by z_h and all its K nearest neighbors as the sampling set $S(z_h)$, which as Fig. 3 shows, so we can infer the total number of all possible paired tangent vector (\mathbf{p}, \mathbf{q}) combinations is $\|S(z_h)\| = \sum_{r=1}^{K-1} r$.

In the experiment, we choose $K=7\sim 10$ for all algorithms that need to use the K -neighbor parameter.

With the above sampling method, in order to reduce the computational cost, we simplified the loss function of the model in the experiment. For the simplified isometric loss $\mathcal{L}_{is}(\omega)$, we have:

$$\mathcal{L}_{is}(\omega) = \mathbb{E}_Z \left\{ \frac{1}{\sum_{r=1}^{K-1} r} \sum_{\mathbf{p}, \mathbf{q} \sim S(z_h)} [\mathcal{G}_M^\omega[\mathbf{p}, \mathbf{q}]_{U_{z_h}} - \langle df_D^\theta(\mathbf{p})_{U_{z_h}}, df_D^\theta(\mathbf{q})_{U_{z_h}} \rangle_{\mathbb{R}^d}]^2 \right\} \quad (23)$$

where \mathbf{p} and \mathbf{q} are paired tangent vector combinations selected from the sampling set $S(z_h)$.

A. Geometric-Preserving Evaluation

We compared the new model with 12 baselines using 6 well-recognized geometric structure preservation evaluation metrics: Triplet[42], SpearCor[45], Npp[45], Nnwr[42],

> REPLACE THIS LINE WITH YOUR MANUSCRIPT ID NUMBER (DOUBLE-CLICK HERE TO EDIT) <

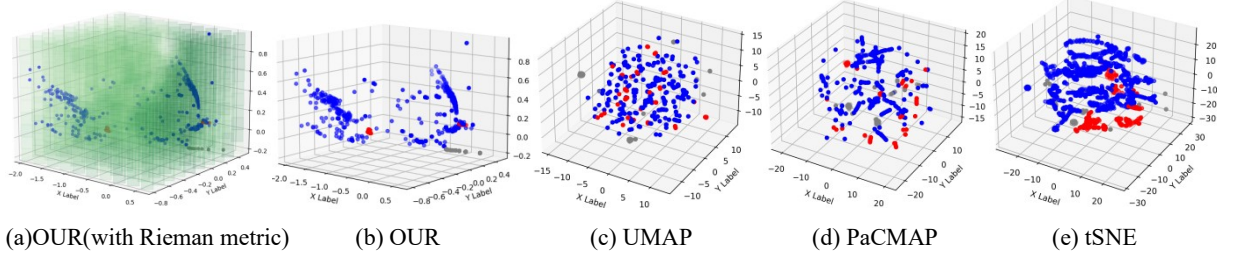


Figure 6: Reduce the dimension of CIC-IDS2018 to a 3D manifold using different methods. We use different colors of point to represent different traffic labels in data, in which red is SSH-attack , gray is FTP-attack, blue is safe traffic

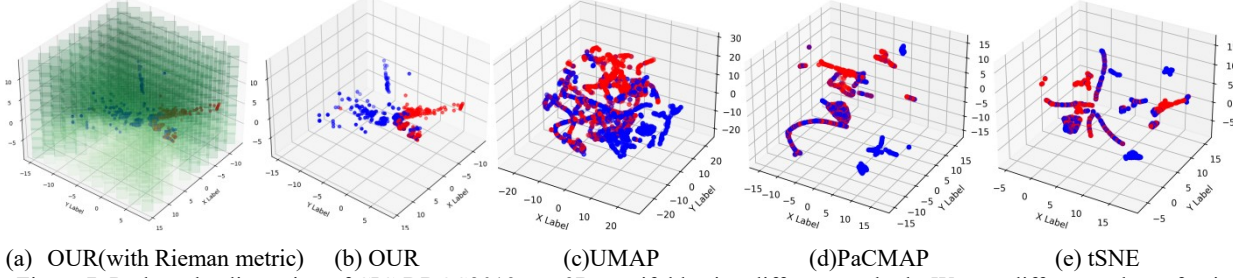


Figure 7: Reduce the dimension of CIC-DDOS2019 to a 3D manifold using different methods. We use different colors of point to represent different traffic labels in data, in which red is attack traffic, blue is safe traffic

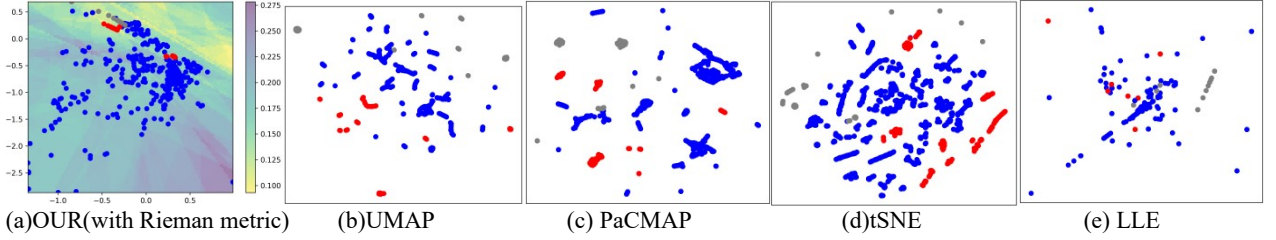


Figure 8: Visualization of CIC-IDS2018 after reducing it to a 2D manifold using different methods

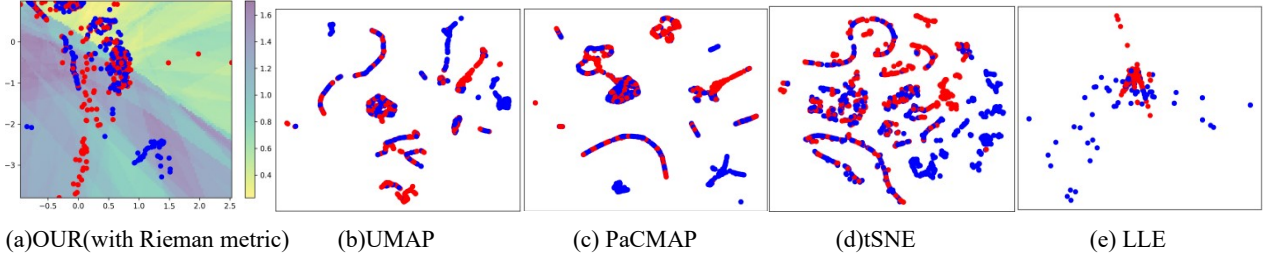


Figure 9: Visualization of CIC-DDOS2019 after reducing it to a 2D manifold using different methods

Auc[46], Curv_sim[42]. We divide these metrics into three categories according to Liu's paper: local geometric property preservation (Npp, Nnwr), global geometric property preservation (Triplet, SpearCor), both local and global property preservation (Auc), and Riemann curvature structure preservation (Curv_sim). The Fig. 4~9 showed the visualization results on 3- and high-dimensional datasets. To more intuitively visualize the position-dependent Riemann metric learned by the model, the heatmaps in Fig. 6 to 9 represented the average modulus length of all unit basis vectors calculated under the learned Riemann metric at different positions (the darker the color, the longer the unit modulus). Table 3 provided the geometric-preserving evaluation results on the CIC-IDS2018, with the evaluation metric scores range from 0 to 1, where values closer to 1 indicate better performance. We highlight the top three best

methods and calculate the average score for each evaluation metric. From the experimental results, it could be seen that the new model achieves outstanding results under most evaluation metrics. It is worth noting that, the new model consistently obtained the highest average metric score compared with the other 10 baselines in all datasets.

The existing manifold learning evaluation methods mainly focus on the invariance of data in terms of topological relationships, such as the preservation of adjacency relationships between samples. However, as analyzed earlier, the inner product plays a crucial role in geometric relationship expression and has a strong mathematical interpretability. Despite this, there is currently no standard metric for quantifying inner product relationships. To address this, we propose the Inner Product Invariance (IPI) metric, specifically designed for evaluating the preservation of geometric

> REPLACE THIS LINE WITH YOUR MANUSCRIPT ID NUMBER (DOUBLE-CLICK HERE TO EDIT) <

Datasets	DLR-F11	σ	TOSCA-Cat	σ	TOSCA-Human	σ	TOSCA-Gorilla	σ
LLE	1.010E+00	95.36%	9.997E-01	83.79%	1.002E+00	92.76%	9.987E-01	87.84%
MLLE	1.011E+00	95.37%	1.000E+00	83.79%	1.002E+00	92.76%	9.988E-01	87.84%
LTSA	1.733E+00	97.30%	1.000E+00	83.79%	1.002E+00	92.76%	1.184E+00	89.75%
ISOMAP	1.027E+00	95.44%	1.036E+00	84.36%	5.509E-01	86.83%	6.138E-01	80.22%
Spectral	1.013E+00	95.38%	1.000E+00	83.80%	1.003E+00	92.77%	9.999E-01	87.86%
inv_ML	1.888E-01	75.19%	2.345E-01	30.88%	8.290E-01	91.25%	3.016E-01	59.74%
DTR_AE	6.391E-01	92.67%	5.815E-01	72.12%	6.966E-01	89.58%	2.453E+00	95.05%
OURS	4.685E-02	-	1.621E-01	-	7.256E-02	-	1.214E-01	-
AVG	-	92.38%	-	74.65%	-	91.24%	-	84.04%

Table 4: IPI comparison experiment on 3-dimensional datasets

Datasets	CIC-IDS2018				CIC-DDoS2019			
Dimension	3D-Manifold	σ	4D-Manifold	σ	3D-Manifold	σ	4D-Manifold	σ
LLE	1.001E+00	97.52%	1.001E+00	97.54%	1.007E+00	88.07%	1.007E+00	97.77%
MLLE	1.001E+00	97.52%	1.001E+00	97.54%	1.007E+00	88.07%	1.007E+00	97.77%
LTSA	1.001E+00	97.52%	1.001E+00	97.54%	1.003E+00	88.03%	1.007E+00	97.77%
ISOMAP	2.374E-01	89.54%	2.696E-01	90.88%	3.566E-01	66.33%	3.156E-01	92.88%
Spectral	1.001E+00	97.52%	1.001E+00	97.54%	1.007E+00	88.07%	1.007E+00	97.77%
CAMEL	1.002E+00	97.52%	1.001E+00	97.54%	9.719E-01	87.64%	9.550E-01	97.65%
PaCMAP	1.004E+00	97.52%	1.002E+00	97.55%	1.003E+00	88.03%	1.007E+00	97.77%
UMAP	1.001E+00	97.52%	1.001E+00	97.54%	1.003E+00	88.03%	1.006E+00	97.77%
inv_ML	2.525E-01	90.16%	8.160E-01	96.99%	8.653E-01	86.12%	8.417E-01	97.33%
DTR_AE	1.001E+00	97.52%	1.000E+00	97.54%	1.005E+00	88.05%	1.005E+00	97.76%
OURS	2.484E-02	-	2.460E-02	-	1.201E-01	-	2.247E-02	-
AVG	-	95.98%	-	96.82%	-	85.64%	-	97.22%

Table 5: IPI comparison experiment on high-dimensional datasets

structures in manifold learning. We quantify IPI with \mathcal{L}_{is} in (14), where f_D^{θ} represent the specific manifold learning method. At the same time, from the equivalent (4) of kernel function and isometric mapping, it can be seen that IPI is also a measure of kernel function loss. The closer the IPI is to 0, the better the inner product invariance of the kernel is. It should be noted that, traditional manifold learning baselines do not have the ability to conduct metric learning. As a result, the metric \mathcal{G}_M^{ω} on their learned manifold \mathcal{M} is the Euclidean metric (identity matrix) everywhere, and we set π for these methods using the K -nearest neighbor algorithm. We use $\sigma = \frac{\|\mathcal{L}_{is}^{our} - \mathcal{L}_{is}^{method}\|}{\mathcal{L}_{is}^{method}}$ to calculate the reduction rate of the new method in the IPI metric compared to other methods, and all training data involved in this experiment have been standardized. The new method achieved the best IPI metric proposed in this paper, and as shown in the table 4~5, the reduction rate was close to 90% compared with other manifold learning methods.

These experimental results fully demonstrated the effectiveness of the new model in the premise of maintaining geometric properties. Whether using the geometry-preserving metric recognized by previous researchers or the IPI metric proposed in this paper, the new method outperformed other geometry-preserving manifold algorithms, demonstrating its

superior ability to preserve geometric properties compared to the aforementioned SOTA methods.

B. Downstream Tasks of The Learned Riemann Metric

The new model provides the ability to isometrically induce Riemannian metric, thus constructs Riemannian manifolds for latent representations. The learned Riemannian metric prove that the new model maps discrete non-Euclidean data to a latent space that conforms to the Riemannian manifold, and is also a character that distinguishes the new method from other manifold learning methods. We believe that the Riemannian metric contains the intrinsic geometric information between samples in the original space, so that the model can still maintain the geometric patterns of data, after reducing its dimension. However, the Riemannian metric is a tensor that does not possess constant components that can be compared. Therefore, we evaluate the practicality of the metric learned by the new model through its efficacy on downstream tasks, indicating the inherent geometric information it contains.

a. Discrete sample reconstruction

To evaluate the impact of the learned Riemannian metric on downstream tasks, we referred to a research in the field of intelligent aerodynamics, which used 2-dimensional manifold metric to reconstruct 3-dimensional wing shapes in European

> REPLACE THIS LINE WITH YOUR MANUSCRIPT ID NUMBER (DOUBLE-CLICK HERE TO EDIT) <

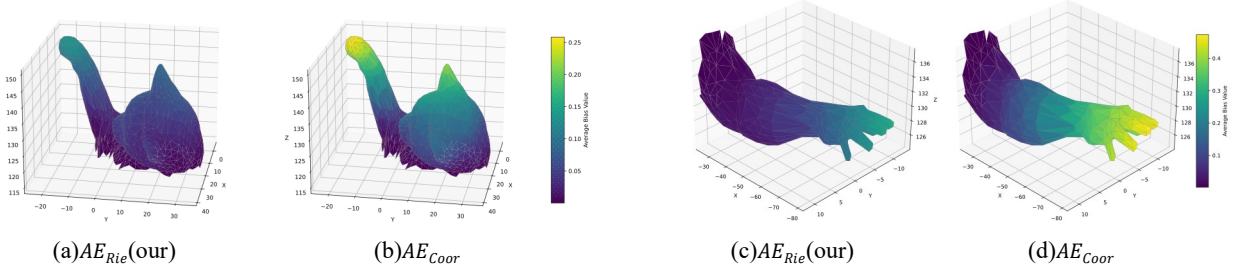


Figure 10: We use heatmaps to show the effect of reconstructing a 3D model using the learned Riemannian metric or using only spatial coordinates under the same AE. The lighter the colorbar, the greater the MSE error of the reconstruction. Sub-figs (a) and (b) are the reconstruction results of the Cat point cloud in TOSCA. Sub-figs(c) (d) are reconstruction of human's hand.

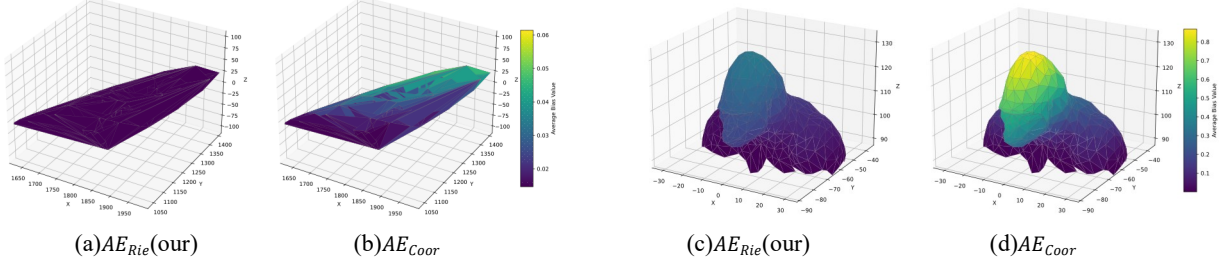


Figure 11: Sub-figs (a) and (b) are the reconstruction results of the foil point cloud in DRL-F11. (c) (d) is a comparison of gorilla reconstruction. The lighter the colorbar, the greater the MSE error of the reconstruction.

Datasets	DLR-F11			TOSCA-Cat			TOSCA-Human		
Valid-Train Ratio	\mathcal{L}_{AE_Rie}	\mathcal{L}_{AE_Coor}	η	\mathcal{L}_{AE_Rie}	\mathcal{L}_{AE_Coor}	η	\mathcal{L}_{AE_Rie}	\mathcal{L}_{AE_Coor}	η
0.2	2.78E-05	1.80E-04	84.52%	5.93E-05	1.95E-04	69.63%	5.93E-05	2.70E-04	78.01%
0.4	5.83E-04	9.40E-04	38.01%	2.26E-03	3.25E-03	30.36%	1.93E-03	2.88E-03	32.88%
0.6	1.51E-02	2.88E-02	47.47%	1.30E-01	1.74E-01	25.19%	5.46E-02	6.96E-02	21.49%
0.8	4.28E-01	5.81E-01	26.33%	3.94E-01	5.30E-01	25.77%	1.14E-01	1.57E-01	27.64%
AVG	1.11E-01	1.53E-01	49.08%	1.32E-01	1.77E-01	37.74%	4.26E-02	5.75E-02	40.00%

Table 6: The reconstruction experiments on 3-D datasets, set the validation training ratio range from 0.2~0.8.

Space[47]. This section compares the utilization of spatial coordinates or Riemannian metric as input features in the reconstruction model to rebuild the discrete data distribution in the validation set, thus demonstrating that the Riemannian metric contains geometric pattern in the original space.

Regarding the choice of geometry reconstruction model, the AE have emerged as a pivotal tool in the reconstruction and restoration of point cloud datasets, leveraging their ability to learn compact representations from complex data. Various models, including masked and implicit AE, have been developed to enhance the accuracy and efficiency of point cloud reconstruction[48]. Consequently, we developed two AE for the downstream reconstruction work. Reconstruction model AE_{Rie} utilizes the Riemannian metric learned from the upstream model as part of input feature, concatenating it with the coordinates from the original space before inputting it into the model for data reconstruction. In contrast, reconstruction model AE_{Coor} solely inputs the coordinates from the original space as a input feature.

We choose mean square error (MSE) as the loss function for the AE:

$$\begin{cases} \mathcal{L}_{AE_Coor} = \frac{1}{N} \sum_{h=1}^N (AE_{Coor}(\mathcal{C}_h) - \mathcal{C}_h)^2 \\ \mathcal{L}_{AE_Rie} = \frac{1}{N} \sum_{h=1}^N (AE_{Rie}(\mathbf{r}_h) - \mathcal{C}_h)^2 \end{cases}$$

Where \mathcal{L}_{AE} denotes the reconstruction loss of the model, AE represents the mapping function of the autoencoder, \mathcal{C}_h states the original space coordinate encoding of the h th discrete sample, and \mathbf{r}_h represents the concatenated features of the Riemann metric learned from the upstream and spatial coordinate $\mathbf{r}_h = [\text{flatten}(G|_{U_h}) \parallel \mathcal{C}_h]$. We use η to represent the MSE reduction rate:

$$\eta = \frac{\|\mathcal{L}_{AE_Coor} - \mathcal{L}_{AE_Rie}\|}{\|\mathcal{L}_{AE_Coor}\|}$$

We conducted data reconstruction experiments on both high-dimensional datasets and 3-dimensional datasets. In the upstream isometric immersion kernel learning, we mapped the 68-dimensional CIC-IDS2018 dataset and the 69-dimensional CIC-DDoS2019 dataset to 3-dimensional and 4-dimensional Riemann manifolds respectively. The 3D point cloud datasets are mapped to a 2D manifold, and all the trained mapping functions f_ϕ^ω were recorded to facilitate downstream tasks to calculate the Riemann metric at any spatial coordinate

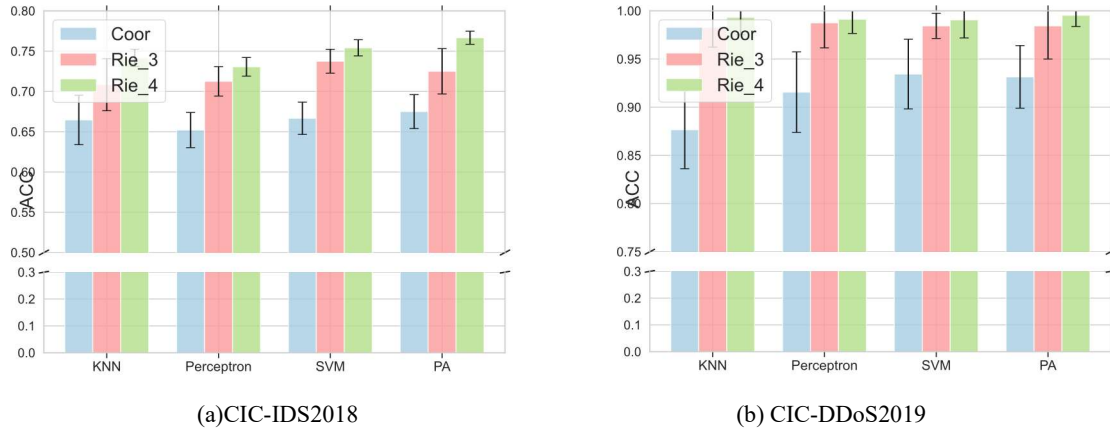


Figure 12: We compared the downstream Multiple-classification accuracy of the reconstructed data using the learned Riemannian metri (Rie_3, Rie_4) and using the spatial coordinates(Coor). The blue, pink, green column represents the accuracy of downstream classification tasks after reconstructing data using the original Euclidean space coordinates(AE_{Coor}), the learned Riemannian metric of a 3l manifold(AE_{Rie_3}), and the learned Riemannian metric of a 4D manifold(AE_{Rie_4})

Datasets	CIC-DDoS2019					CIC-IDS2018				
Dimensions	AE_{Coor}	AE_{Rie_3}	η	AE_{Rie_4}	η	AE_{Coor}	AE_{Rie_3}	η	AE_{Rie_4}	η
Knn	66.46%	70.83%	6.58%	74.17%	11.60%	87.66%	98.28%	12.12%	99.32%	13.31%
Perceptron	65.21%	71.25%	9.27%	73.06%	12.03%	91.56%	98.75%	7.85%	99.12%	8.26%
SVM	66.67%	73.75%	10.62%	75.42%	13.12%	93.44%	98.44%	5.35%	99.06%	6.02%
PA	67.50%	72.50%	7.41%	76.67%	13.58%	93.15%	98.44%	5.68%	99.54%	6.87%
AVG	66.46%	72.08%	8.47%	74.83%	12.58%	91.45%	98.48%	7.75%	99.26%	8.61%

Table 7: Tabulate the data in Fig. 12 to compare the classification accuracy of various classification algorithms.

according to (13).

In the downstream reconstruction experiment, we observed the data reconstruction accuracy of the AE at different validation-training ratios. Compared with the model AE_{Coor} that only used coordinates as input features, the AE_{Rie} model's reconstruction accuracy of the CIC-IDS2018 dataset was improved by 12.85% and 18.32% on average with the assistance of 3-dimensional Riemannian metric and 4-dimensional Riemannian metric, and the reconstruction accuracy of the CIC-DDoS2019 dataset was improved by 8.44% and 10.42% respectively. the downstream accuracy improvement on low-dimensional datasets is more obvious. We conducted reconstruction experiments on the DLR-F11, TOSCA-Cat and TOSCA-Human 3-dimensional point cloud datasets. The results are shown in Table 6, using the 2-dimensional Riemannian metric as input feature, the reconstruction accuracy of the AE_{Rie} increased by about 40% on average.

We show a visual comparison of the reconstruction accuracy of AE_{Rie} and AE_{Coor} on the 3-dimensional datasets in Fig. 10, 11. We used heatmaps to represent the reconstruction accuracy loss \mathcal{L}_{AE} at different spatial positions. we see that AE_{Rie} had higher reconstruction accuracy than AE_{Coor} at positions with more geometric details, such as the hands in TOSCA-Human and the cat's paw in TOSCA-Cat.

For high-dimensional data, studies have shown that accurate reconstruction and generation of high-dimensional data

significantly enhance the performance of downstream tasks across various domains[49]. We conducted downstream classification accuracy comparison experiments on the reconstructed data of two groups of high-dimensional point cloud datasets on the validation set, and found that the classification effect of high-dimensional data reconstructed by the AE_{Rie} with Riemannian metric as input feature is better than the data reconstructed by the AE_{Coor} with only coordinates as input features.

The results of the classification experiment are illustrated in the Fig. 12 and Table 7. In the upstream task, we employed the IIKL model to map high-dimensional data to 3-dimensional or 4-dimensional Riemannian manifolds. Subsequently, in the downstream task, we utilized the Riemannian metric on the low-dimensional manifold as input features and conducted downstream classification on the rebuilt data within the validation set. The accuracy of the validation set reconstructed with the aid of the Riemannian metric was superior to that of the validation set with solely coordinate reconstruction. In the downstream task, We selected 4 recognized classification algorithms (KNN[50], Perceptron[51], SVM[52], PA[53]) to classify the reconstructed data and calculate the classification accuracy. The classification accuracy of the validation set reconstructed using Riemannian metric assistance was enhanced by approximately 10% compared to the validation set reconstructed solely with coordinates. Furthermore, the downstream classification accuracy of the validation set

Datasets	CIC-IDS2018				CIC-DDoS2019			
	Conformal-Preserving	σ	Isometry-Preserving	σ	Conformal-Preserving	σ	Isometry-Preserving	σ
LLE	1.32E+00	98.06%	1.05E+00	82.16%	1.01E+00	89.40%	8.20E-01	80.76%
MLLE	1.32E+00	98.06%	1.40E+00	86.68%	1.01E+00	89.40%	1.03E+00	84.66%
LTSA	1.11E+00	97.69%	1.97E+00	90.49%	1.00E+00	89.31%	2.36E-01	33.24%
ISOMAP	5.53E-01	95.36%	1.10E+00	83.03%	9.11E-01	88.24%	8.28E-01	80.93%
Spectral	1.50E+00	98.29%	1.12E+00	83.33%	1.01E+00	89.40%	1.37E+00	88.47%
CAMEL	1.70E+00	98.49%	1.66E+00	88.72%	9.50E-01	88.73%	1.22E+00	87.08%
PaCMAP	1.08E+00	97.63%	1.51E+00	87.64%	1.00E+00	89.33%	8.25E-01	80.88%
UMAP	1.00E+00	97.44%	1.49E+00	87.43%	1.01E+00	89.38%	7.58E-01	79.17%
Inv_ML	2.55E-01	89.94%	2.61E-01	28.33%	9.02E-01	88.12%	2.11E-01	25.18%
DTR_AE	1.00E+00	97.43%	2.41E-01	22.45%	1.01E+00	89.39%	1.75E-01	9.92%
OURS	2.57E-02	-	1.87E-01	-	1.07E-01	-	1.58E-01	-
AVG	-	96.84%	-	74.02%	-	89.03%	-	71.15%

Table 8: Experiments on the model's conformal and isometry properties.

reconstructed with 4D Riemannian metric assistance was marginally superior to that of the validation set reconstructed with 3D assistance. We believe this may be due to the inevitable loss of intricate patterns when reducing high-dimensional data to low-dimensional manifolds, whereas higher-dimensional manifolds might more effectively preserve these geometric features.

The experimental results demonstrated that the Riemannian metric learned by the new model not only preserved geometric relationships but also significantly boosted the performance of downstream tasks, enhancing the accuracy and robustness of both reconstruction and classification tasks. This underscored the potential of the proposed method in maintaining the underlying geometric properties of non-Euclidean data and improving the quality of representation learning across a range of applications.

b. Preservation of geometric properties related to inner products

The invariance of the inner product of vectors is essential for preserving the geometric properties of non-Euclidean discrete data, especially in applications aimed at retaining isometric and conformal representations. This invariance ensures that transformations of the spatial coordinate system in which the data reside do not change the underlying physical relationships within the data, which is critical for accurate representation.

Specifically, we derived two quantifiable geometric metrics: isometry preservation and conformal preservation, and validated the new model's ability to maintain the geometric properties. Regarding isometry preservation, the vector modulus in high-dimensional space can be considered the distance between two points, and the modulus of a vector can be computed using its inner product $\|q\| = \sqrt{\langle q, q \rangle}$. Consequently, we propose quantifying the modifications in the modulus of the identical before and after manifold learning to assess the distance preservation. In terms of conformal

preservation, the formula for calculating the cosine angle between two vectors p, q can be calculated based on their inner product and modulus $\cos\theta = \frac{p \cdot q}{\|p\| \cdot \|q\|}$. Similarly, we quantify the angle modifications of the same two vectors to measure the conformal preservation of manifold learning. We used the following formula to calculate the conformal preservation loss and isometry preservation loss of the model in the following experiment.

$$\mathcal{L}_{iso} = \mathbb{E}_Z \left\{ \frac{1}{K} \sum_{q \sim S(z_h)} [\mathcal{G}_M^\omega[q, q]_{U_{z_h}} - \langle df_D^\theta(q)_{U_{z_h}}, df_D^\theta(q)_{U_{z_h}} \rangle_{\mathbb{R}^d}]^2 \right\} \quad (24)$$

$$\mathcal{L}_{con} = \mathbb{E}_Z \left\{ \frac{1}{\sum_{r=1}^{K-1} r} \sum_{p, q \sim S(z_h)} \left[\frac{\mathcal{G}_M^\omega[p, q]_{U_{z_h}}}{\mathcal{G}_M^\omega[p, q]_{U_{z_h}}^{\frac{1}{2}} \cdot \mathcal{G}_M^\omega[p, q]_{U_{z_h}}^{\frac{1}{2}}} - \frac{\langle df_D^\theta(p)_{U_{z_h}}, df_D^\theta(q)_{U_{z_h}} \rangle_{\mathbb{R}^d}}{\|df_D^\theta(p)_{U_{z_h}}\| \cdot \|df_D^\theta(q)_{U_{z_h}}\|} \right]^2 \right\} \quad (25)$$

The above two equations are derived from equation (23) concerning the invariance of the metric inner product, where df_D^θ denotes the mapping function of manifold learning, $\langle \cdot, \cdot \rangle_{\mathbb{R}^d}$ signifies the inner product operation of two vectors in Euclidean space, $\mathcal{G}_M^\omega[\cdot, \cdot]_{U_{z_h}}$ indicates the inner product between two vectors under the Riemannian metric \mathcal{G}_M^ω at point z_h , and $\|\cdot\|$ represents the modulus calculation in Euclidean space. It should be noted that except for our model, other manifold learning methods reduce the original data to a low-dimensional Euclidean space, so \mathcal{G}_M^ω represents the Euclidean metric in these methods.

The results in Table 8 demonstrated that our model significantly outperformed existing manifold learning approaches regarding conformal and isometry preservation. The isometry preservation losses on the CIC-DDoS2019 and CIC-IDS2018 datasets were enhanced by an average of 89.15% and 97.63%, respectively, relative to other methods.

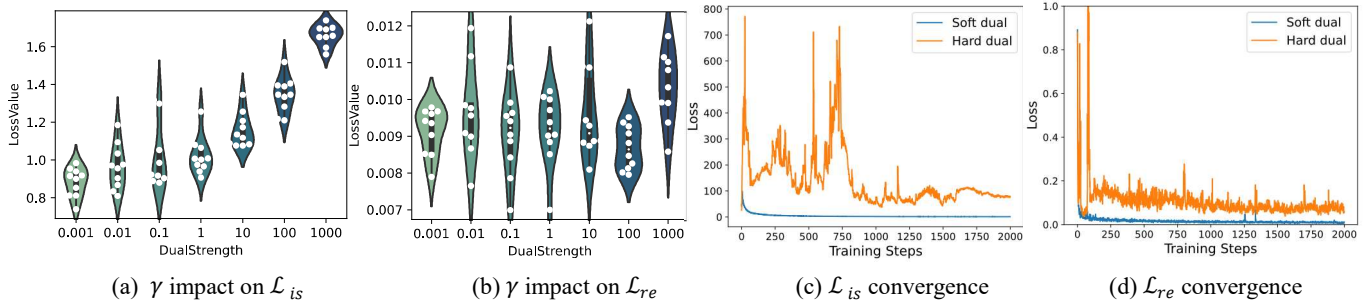


Figure 13: In sub-Fig(a),(b) The impact of dual ablation on model’s learning objectives. White dots represent a training instance. In sub-Fig(c),(d) We set $\gamma=0.1$ for the soft-dual model (blue) to compare the loss convergence trend with the hard-dual model (orange). The sub-Fig(c) shows the isometric loss convergence, and the sub-Fig(d) shows the immersion loss convergence.

Dual Strength γ	10^{-1}	10^0	10^1	10^2	10^3	Hard*
Convergence probability	100%	100%	100%	98%	95%	57%

Table 9: The influence of different dual strength γ on model’s convergence probability.

“Hard*”: Represents the hard-dual model

The conformal preservation losses were also enhanced by 74.36% and 30.45% on the two datasets respectively compared with these manifold learning methods.

These experimental results highlighted the effectiveness of the learned Riemannian metric in preserving key geometric properties— isometric and conformal representations, within the tangent space during manifold learning. By adhering to the inner product invariance constraint, the model ensure that the intrinsic geometric patterns of the data are retained, even in lower-dimensional representations. This not only improved the accuracy and fidelity of the learned manifold but also enhanced the performance of geometric-metrics based downstream tasks, where the preservation of physical relationships is critical.

C. Model Validity Studies

a. Soft-dual ablation

The model’s soft-dual ablation studies on DLR-F11 dataset are shown in Fig. 13. The correlation between the hyperparameter γ , which controls the soft-dual loss strength, and the isometric property of the model is clearly apparent. The weaker the dual bond was, the lower the isometric loss \mathcal{L}_{is} was. Relatively, the dual bond has a smaller impact on immersion loss \mathcal{L}_{re} . It is important to note that we also conducted the same experiment on models that did not employ the soft-dual trick(hard-dual model). The average \mathcal{L}_{is} and \mathcal{L}_{re} of these models were around 10 times higher on average compared to those that utilized soft-dual trick.

In addition, the influence of different soft-dual strengths on the model’s convergence probability was statistically analyzed as shown in Table 9. As implied, after 50 times independent 2K iterations training for each soft-dual strength model on DLR-F11 dataset, the stronger the dual bond between f_D^θ and f_ϕ^ω , the lower the convergence probability of the model. When the model did not equip with the soft-dual trick, the average convergence probability was only 57%.

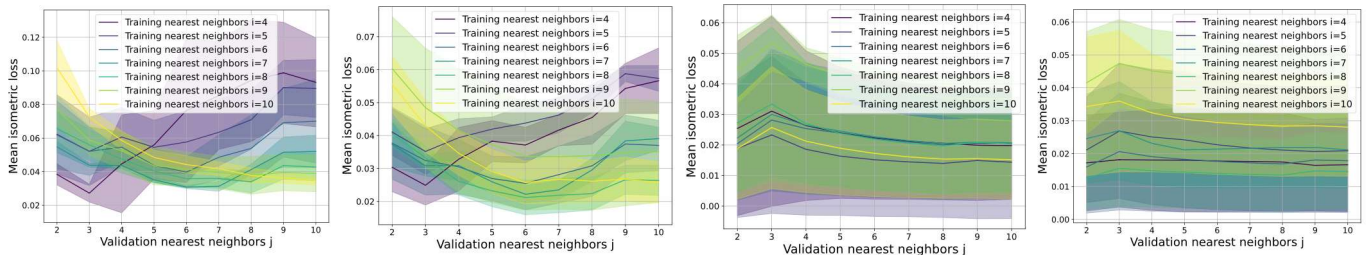
The experimental results proved the necessity and feasibility of soft-dual module for model convergence.

b. Generalization of the kernel in tangent space

We conducted an experiment to investigate the influence of the K setting in the approximate tangent space on the generalization of the kernel function. The Riemann metric as the inner product metric of the kernel function is a symmetric metric matrix of $n \times n$ dimensions, where n represents the dimension of the Riemannian manifold. Theoretically, only $n+1$ different vectors in the tangent space are needed to pair-combine a set of inner product equations (total $\sum_{m=1}^n m$ equations) to obtain the unique solution of the Riemannian metric matrix, i.e. according to the sampling set construction method mentioned in (23), $\|S(z_h)\| = \sum_{r=1}^{K-1} r = \sum_{m=1}^n m$ is required, that is, when the original data is reduced to an n -dimensional manifold \mathcal{M} , setting $K = n + 1$ is enough for the model to learn the unique Riemann metric in arbitrary tangent space on \mathcal{M} . Although this result could be achieved in theory, we are concerned that modifying the setting of K neighbors may influence the generalization of the model in practical. Consequently, in this experiment, we assumed that each sample z_h possesses 10 nearest neighbors to establish its approximate tangent space. However, during training, we would utilize only the i training nearest neighbors ($i \leq 10$) with the top minimal distance from the origin sample z_h to construct the tangent vector set $S(z_h)$, which contribute to the learning of the Riemannian metric. Subsequently, we assessed the impact of varying choices of i on the generalization performance of the Riemannian metric by verifying the model’s isometric loss performance under different numbers of validation nearest neighbors j ($j \leq 10$, which also represents the j neighbor samples with the top minimal distance from the origin sample z_h) in the tangent space.

We conducted two groups of experiments in high-dimensional datasets. In CIC-IDS2018, we standardized the

> REPLACE THIS LINE WITH YOUR MANUSCRIPT ID NUMBER (DOUBLE-CLICK HERE TO EDIT) <



(a)DDoS2019 to 3D manifold (b)DDoS2019 to 4D manifold (c)IDS2018 to 3D manifold (d) IDS2018 to 4D manifold
Figure 14: Generalization experiment of kernel function in tangent space

discrete data before training, while in CIC-DDoS2019, we did not pre-process the training data. Sub-Figures 14 (a),(b) show the experiments of reducing the 69-dimensional CIC-DDoS2019 data to a 3- and 4-dimensional Riemannian manifold. We could see that when i was close to 10, the Riemannian metric's accuracy in predicting the inner product relationship between the nearest samples decreased. When i was small, the learned Riemannian metric had poor generalization performance in predicting the inner product relationship between samples with larger j (samples far from the origin). This indicated that as i approaches j , the Riemannian metric in tangent space had better generalization, thus, the kernel's inner product invariance improved; conversely, when they were farther apart, the kernel's generalization weakens. Sub-figures 14 (c) and (d) show the experimental results of reducing the dimensionality of the samples in the CIC-IDS2018 dataset to 3- and 4-dimensional Riemann manifolds. In comparison to the unstandardized data, the validation nearest neighbors j showed a lower impact on the kernel's generalization, with the model mainly affected by the K configuration. The comparison between these two groups results showed that normalizing the original data could enhance the kernel's robustness to attain inner product invariance within the tangent space.

In addition, we can conclude that the kernel function learned by the model has a certain generalization in the tangent space, but in actual training we should choose the K appropriately. An overly large or small K will influence the kernel's generalization performance. From the above experiments, it can be inferred that the K slightly larger than the theoretical value $n + 1$ ($K = n + 2 \sim n + 3$) is a better choice.

VI. CONCLUSION

In this paper, we introduce the concept of Isometric Immersion Kernel Learning (IIKL), which aims to preserve the geometric properties of discrete data in a self-supervised manner. By leveraging Riemannian geometry as an inductive bias, our method ensures that transformations of the spatial coordinate system are accompanied by the preservation of inner product invariance in the tangent space. This new model eliminates the need for prior assumptions about manifold distribution, providing a more general and robust method for manifold learning. During the research process, we found the gap between theory and practice, which leads to model convergence issues. To address this, we introduce a soft-dual

module based on maximum likelihood estimation theory, ensuring stable and effective training convergence of the new model.

Through extensive experiments on 3D and high-dimensional discrete datasets, we demonstrated the superior performance of our approach in preserving geometric properties compared to existing SOTA methods. Specifically, our proposed Inner Product Invariance (IPI) metric quantitatively showed that our method reduces the loss in isometric and conformal tasks related to inner product invariance by over 80% compared to other geometry-preserving manifold methods. Additionally, downstream tasks leveraging the learned Riemannian metrics exhibited improved performance, highlighting the practical utility of our model in real-world applications.

At present, our model studies the extraction of latent representations that satisfy inner product invariance from finite-dimensional discrete data whose original space is assumed Euclidean space. In the future research, we intend to broaden the variety of kernel functions that facilitate inner product invariance, evaluate the effects of extra kernel functions on downstream tasks, and implement the Riemannian metric learned by the model in more complex application scenarios (such as atmospheric physical parameters in high-dimensional space and infinite-dimensional feature data) for scientific representation analysis.

REFERENCES

- [1] H. Wang, T. Fu, Y. Du, W. Gao, K. Huang, Z. Liu, P. Chandak, S. Liu, P. Van Katwyk, A. Deac, Scientific discovery in the age of artificial intelligence, *Nature* 620(7972) (2023) 47-60.
- [2] F. Boso, D.M. Tartakovsky, Information geometry of physics-informed statistical manifolds and its use in data assimilation, *Journal of Computational Physics* 467 (2022) 111438.
- [3] B. Quackenbush, P. Atzberger, Geometric Neural Operators (GNPs) for data-driven deep learning in non-euclidean settings, *Machine Learning: Science and Technology* (2024).
- [4] M. Meilä, H. Zhang, Manifold learning: What, how, and why, *Annual Review of Statistics and Its Application* 11 (2024).
- [5] W. Choi, M. Shin, S. Im, Depth-discriminative metric learning for monocular 3D object detection, *Advances in Neural Information Processing Systems* 36 (2024).
- [6] N. Liu, Y. Yu, H. You, N. Tatikola, Ino: Invariant neural operators for learning complex physical systems with momentum conservation, *International Conference on Artificial Intelligence and Statistics*, PMLR, 2023, pp. 6822-6838.
- [7] C. Li, Z. Liu, B. Shou, Inner Product of Irreducible Finite-dimensional Representations of Classical Groups, *arXiv preprint arXiv:1803.02679* (2018).
- [8] S.H. Sababe, On 2-inner product spaces and reproducing kernel property, (2019).

- [9] X. Ding, R. Ma, Learning low-dimensional nonlinear structures from high-dimensional noisy data: An integral operator approach, *The Annals of Statistics* 51(4) (2023) 1744-1769.
- [10] Y. Zhou, C. Chen, J. Xu, Learning manifold implicitly via explicit heat-kernel learning, *Advances in Neural Information Processing Systems* 33 (2020) 477-487.
- [11] D.T. Nguyen, K. Slavakis, Multi-linear kernel regression and imputation via manifold learning: The dynamic MRI case, *ICASSP 2024-2024 IEEE International Conference on Acoustics, Speech and Signal Processing (ICASSP)*, IEEE, 2024, pp. 9466-9470.
- [12] C. Soize, R. Ghanem, Transient anisotropic kernel for probabilistic learning on manifolds, *Computer Methods in Applied Mechanics and Engineering* 432 (2024) 117453.
- [13] P. Mostowsky, V. Dutordoir, I. Azangulov, N. Jaquier, M.J. Hutchinson, A. Ravuri, L. Roza, A. Terenin, V. Borovitskiy, The GeometricKernels Package: Heat and Mat\ern Kernels for Geometric Learning on Manifolds, Meshes, and Graphs, *arXiv preprint arXiv:2407.08086* (2024).
- [14] N. Dyn, N. Sharon, A global approach to the refinement of manifold data, *Mathematics of Computation* 86(303) (2017) 375-395.
- [15] D.B. Dunson, N. Wu, Inferring manifolds from noisy data using Gaussian processes, *arXiv preprint arXiv:2110.07478* (2021).
- [16] L. McInnes, J. Healy, J. Melville, Umap: Uniform manifold approximation and projection for dimension reduction, *arXiv preprint arXiv:1802.03426* (2018).
- [17] F. Xie, Y. Fan, M. Zhou, Dimensionality reduction by weighted connections between neighborhoods, *Abstract and Applied Analysis*, Wiley Online Library, 2014, p. 928136.
- [18] C. Geng, J. Wang, L. Chen, W. Bao, C. Chu, Z. Gao, Uniform interpolation constrained geodesic learning on data manifold, *arXiv preprint arXiv:2002.04829* (2020).
- [19] B. Pang, Z. Zheng, G. Wang, P.-S. Wang, Learning the geodesic embedding with graph neural networks, *ACM Transactions on Graphics (TOG)* 42(6) (2023) 1-12.
- [20] Y. Jin, R. McDaniel, N.J. Tatro, M.J. Catanzaro, A.D. Smith, P. Bendich, M.B. Dwyer, P.T. Fletcher, Implications of data topology for deep generative models, *Frontiers in Computer Science* 6 (2024) 1260604.
- [21] Q. Zou, Learning Emotion Representations on a Manifold, 2022 IEEE Conference on Telecommunications, Optics and Computer Science (TOCS), IEEE, 2022, pp. 1431-1435.
- [22] J.D. Tucker, M.T. Martinez, J.M. Laborde, Dimensionality reduction using elastic measures, *Stat* 12(1) (2023) e551.
- [23] Z. Hu, K. Shukla, G.E. Karniadakis, K. Kawaguchi, Tackling the curse of dimensionality with physics-informed neural networks, *Neural Networks* 176 (2024) 106369.
- [24] K. Donhauser, M. Wu, F. Yang, How rotational invariance of common kernels prevents generalization in high dimensions, *International Conference on Machine Learning*, PMLR, 2021, pp. 2804-2814.
- [25] M. Mahmoudi, A. Chetouani, F. Boufera, H. Tabia, Kernel function impact on convolutional neural networks, *arXiv preprint arXiv:2302.10266* (2023).
- [26] T.-Y. Zhou, N. Suh, G. Cheng, X. Huo, Approximation of RKHS Functionals by Neural Networks, *arXiv preprint arXiv:2403.12187* (2024).
- [27] P. Xu, Y. Wang, X. Chen, Z. Tian, Deep kernel learning networks with multiple learning paths, *ICASSP 2022-2022 IEEE International Conference on Acoustics, Speech and Signal Processing (ICASSP)*, IEEE, 2022, pp. 4438-4442.
- [28] P. Dollár, V. Rabaud, S. Belongie, Non-isometric manifold learning: Analysis and an algorithm, *Proceedings of the 24th international conference on Machine learning*, 2007, pp. 241-248.
- [29] S. Shekizhar, A. Ortega, Revisiting local neighborhood methods in machine learning, 2021 IEEE Data Science and Learning Workshop (DSLW), IEEE, 2021, pp. 1-6.
- [30] Z. Chen, W. Wang, Y. Xiang, Isometric Immersion Learning with Riemannian Geometry, *arXiv preprint arXiv:2409.14760* (2024).
- [31] N.S. Dutt, S. Muralikrishnan, N.J. Mitra, Diffusion 3d features (diff3f): Decorating untextured shapes with distilled semantic features, *Proceedings of the IEEE/CVF Conference on Computer Vision and Pattern Recognition*, 2024, pp. 4494-4504.
- [32] J.G. Coder, OVERFLOW analysis of the DLR-F11 high-lift configuration including transition modeling, *Journal of Aircraft* 52(4) (2015) 1082-1097.
- [33] I. Sharafaldin, A.H. Lashkari, S. Hakak, A.A. Ghorbani, Developing realistic distributed denial of service (DDoS) attack dataset and taxonomy, 2019 international carnahan conference on security technology (ICCST), IEEE, 2019, pp. 1-8.
- [34] S.T. Roweis, L.K. Saul, Nonlinear dimensionality reduction by locally linear embedding, *science* 290(5500) (2000) 2323-2326.
- [35] Z. Zhang, J. Wang, MLE: Modified locally linear embedding using multiple weights, *Advances in neural information processing systems* 19 (2006).
- [36] Z. Zhang, H. Zha, Principal manifolds and nonlinear dimensionality reduction via tangent space alignment, *SIAM journal on scientific computing* 26(1) (2004) 313-338.
- [37] L. Van der Maaten, G. Hinton, Visualizing data using t-SNE, *Journal of machine learning research* 9(11) (2008).
- [38] E. Amid, M.K. Warmuth, TriMap: Large-scale dimensionality reduction using triplets, *arXiv preprint arXiv:1910.00204* (2019).
- [39] A. Ng, M. Jordan, Y. Weiss, On spectral clustering: Analysis and an algorithm, *Advances in neural information processing systems* 14 (2001).
- [40] J.B. Tenenbaum, The isomap algorithm and topological stability, *Science* 295(5552) (2002) 7a.
- [41] Y. Wang, H. Huang, C. Rudin, Y. Shaposhnik, Understanding how dimension reduction tools work: an empirical approach to deciphering t-SNE, UMAP, TriMAP, and PaCMAP for data visualization, *Journal of Machine Learning Research* 22(201) (2021) 1-73.
- [42] Y. Liu, Curvature Augmented Manifold Embedding and Learning, *arXiv preprint arXiv:2403.14813* (2024).
- [43] I. Trofimov, D. Cherniavskii, E. Tulchinskii, N. Balabin, E. Burnaev, S. Barannikov, Learning topology-preserving data representations, *ICLR 2023 International Conference on Learning Representations*, 2023.
- [44] S. Li, H. Lin, Z. Zang, L. Wu, J. Xia, S.Z. Li, Invertible manifold learning for dimension reduction, *Machine Learning and Knowledge Discovery in Databases. Research Track: European Conference, ECML PKDD 2021, Bilbao, Spain, September 13-17, 2021, Proceedings, Part III* 21, Springer, 2021, pp. 713-728.
- [45] H. Huang, Y. Wang, C. Rudin, E.P. Browne, Towards a comprehensive evaluation of dimension reduction methods for transcriptomic data visualization, *Communications biology* 5(1) (2022) 719.
- [46] J.A. Lee, D.H. Peluffo-Ordóñez, M. Verleysen, Multi-scale similarities in stochastic neighbour embedding: Reducing dimensionality while preserving both local and global structure, *Neurocomputing* 169 (2015) 246-261.
- [47] Y. Xiang, L. Hu, G. Zhang, J. Zhang, W. Wang, A Manifold-Based Airfoil Geometric-Feature Extraction and Discrepant Data Fusion Learning Method, *IEEE Transactions on Aerospace and Electronic Systems* 59(5) (2023) 6555-6569.
- [48] A.F. Duque, S. Morin, G. Wolf, K.R. Moon, Geometry regularized autoencoders, *IEEE transactions on pattern analysis and machine intelligence* 45(6) (2022) 7381-7394.
- [49] Z. Wang, B. Draghi, Y. Rotalinti, D. Lunn, P. Myles, High-fidelity synthetic data applications for data augmentation, (2024).
- [50] B. Venkateswarlu, R. Gangula, Exploring the Power and Practical Applications of K-Nearest Neighbours (KNN) in Machine Learning, *Journal of Computer Allied Intelligence (JCAI, ISSN: 2584-2676)* 2(1) (2024) 8-15.
- [51] Á. Hajnal, A Perceptron-based Fine Approximation Technique for Linear Separation, *arXiv preprint arXiv:2309.06049* (2023).
- [52] A. Testas, Support Vector Machine Classification with Pandas, Scikit-Learn, and PySpark, *Distributed Machine Learning with PySpark: Migrating Effortlessly from Pandas and Scikit-Learn*, Springer2023, pp. 259-280.
- [53] Y. ZHANG, Learning Label Correlations for Multi-Label Online Passive Aggressive Classification Algorithm, *Wuhan University Journal of Natural Sciences* 29(1) (2024) 51-58.